

Supplementary information: Hydrogen-impurity induced unconventional magnetism in semiconducting molybdenum ditelluride

Jonas A. Krieger,^{1,2,3,*} Daniel Tay,³ Igor P. Rusinov,^{4,5} Sourabh Barua,^{6,†} Pabitra K. Biswas,⁷ Lukas Korosec,³ Thomas Prokscha,¹ Thorsten Schmitt,² Niels B. M. Schröter,^{2,*} Tian Shang,⁸ Toni Shiroka,^{1,3} Andreas Suter,¹ Geetha Balakrishnan,⁶ Evgueni V. Chulkov,^{9,10,4,5} Vladimir N. Strocov,^{2,‡} and Zaher Salman^{1,§}

¹Laboratory for Muon Spin Spectroscopy, Paul Scherrer Institute, CH-5232 Villigen PSI, Switzerland

²Swiss Light Source, Paul Scherrer Institute, CH-5232 Villigen PSI, Switzerland

³Laboratorium für Festkörperphysik, ETH Zürich, CH-8093 Zürich, Switzerland

⁴Tomsk State University, pr. Lenina 36, 634050 Tomsk, Russia

⁵St. Petersburg State University, Universitetskaya nab. 7/9, 199034 St. Petersburg, Russia

⁶Department of Physics, University of Warwick, Coventry CV4 7AL, UK

⁷ISIS Facility, Rutherford Appleton Laboratory, Chilton, Didcot, Oxon OX110QX, United Kingdom

⁸Laboratory for Multiscale Materials Experiments,

Paul Scherrer Institut, CH-5232 Villigen PSI, Switzerland

⁹Donostia International Physics Center, P. Manuel de Lardizabal 4, San Sebastián, 20018 Basque Country, Spain

¹⁰Departamento de Física de Materiales UPV/EHU,

Centro de Física de Materiales CFM - MPC and Centro Mixto CSIC-UPV/EHU, 20080 San Sebastián/Donostia, Spain

Contents

Sample characterization	2
Magnetization measurements	2
ARPES	2
Out-of plane dispersion	2
Static charging	3
n-type samples	4
Density-functional theory calculations	4
Muon spin spectroscopy	5
Zero field angle dependence	5
Low energy μ SR	6
¹²⁵Te-NMR	7
Powder line shapes	7
Spin-lattice relaxation	7
Time scales probed by μ SR and ¹²⁵ Te-NMR	7
References	9

*Current address: Max Planck Institut für Mikrostrukturphysik, Weinberg 2, 06120 Halle, Germany

†Current address: Department of Physics, Central University of Punjab, Bathinda 151401, India

‡Electronic address: vladimir.strocov@psi.ch

§Electronic address: zaher.salman@psi.ch

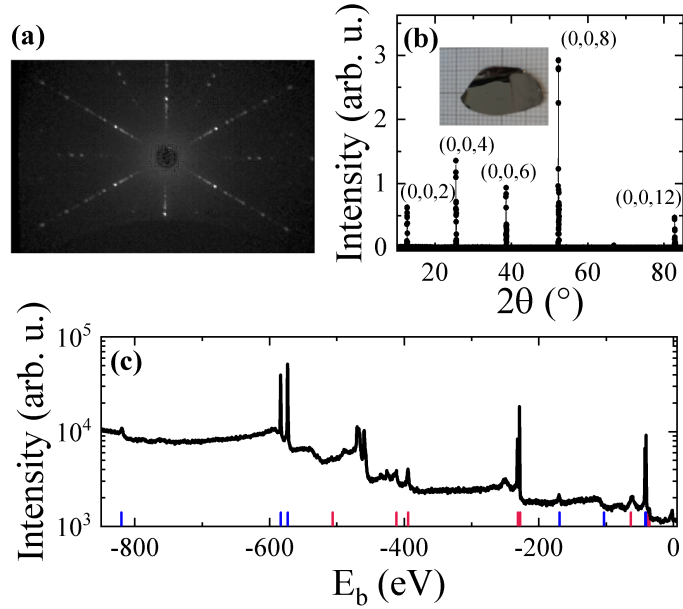


FIG. S1: (a) The Laue back reflection X-ray diffraction pattern for one of the single crystals. (b) X-ray (0,0,n) diffraction peaks. The inset shows a photograph of one of the single crystals. (c) XPS core level spectrum measured at $h\nu = 950$ eV. The blue (red) lines show the expected positions of the Mo (Te) peaks. The additional features around -460 eV are the Te $M_{4,5}$ - $N_{4,5}$ Auger lines.

Sample characterization

Element	Average observed atomic composition (%)	Expected atomic composition (%)
Mo	33.85	33.33
Te	66.14	66.67

TABLE I: Stoichiometry of the sample determined by energy dispersive X-ray spectroscopy.

Magnetization measurements

The magnetometry measurements are shown in Fig. S2. For an applied in-plane field of 100 mT, the sample shows a Curie-Weiss like behavior. In contrast, if the field is applied out-of-plane there is a signature of a transition around 5 K, see Fig. S2(b). Moreover, for an out-of-plane field of 10 mT this transition features a small hysteresis in the magnetization signal, Fig. S2(c). Its magnitude is too small for an intrinsically ferromagnetic sample and it cannot account for the observed magnetic transition in μ SR, which appears at much higher temperatures (~ 40 K). However, it could be attributed to various origins, including magnetic defects [S1] or magnetic grain-boundaries [S2]. Note that a magnetization anomaly was previously observed around 190 K [S1]. The absence of such an anomaly in our sample might be due to a difference in impurities between the two sets of samples, arising from the different growth methods.

ARPES

Out-of plane dispersion

In the soft X-rays energy range the photoelectrons have a larger escape depth compared to standard ultraviolet ARPES. This reduces the k_z broadening and allows to determine the out-of plane dispersion. For a measured

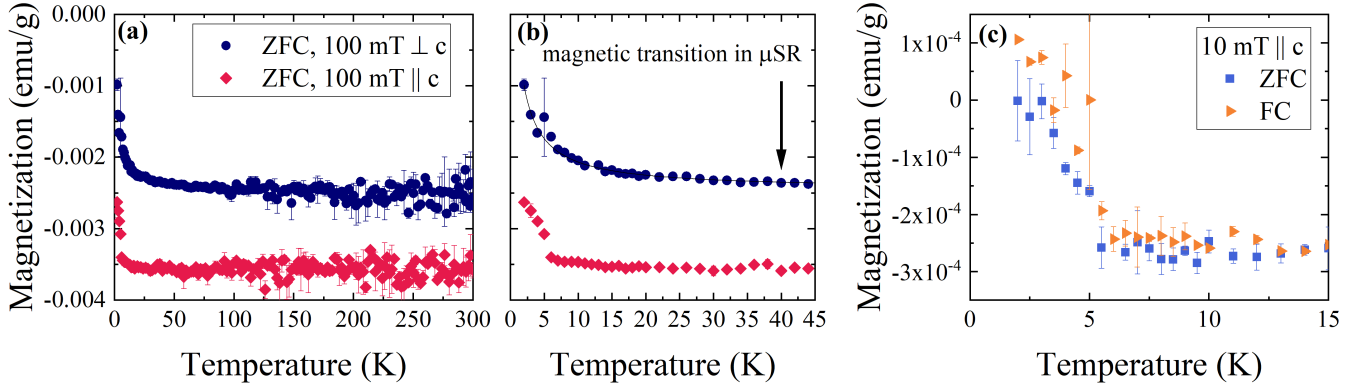


FIG. S2: Magnetization measurements on $2H$ -MoTe $_2$. (a) Zero field cooled (ZFC) magnetization in an applied field of 100 mT. (b) Zoom into the low temperature region of (a). The solid line shows the fit of a Curie-Weiss law ($T_c = -0.9(5)$ K). The arrow shows the onset of the magnetic zero field oscillations observed in μ SR. (c) Field cooled (below 50 K) and zero field cooled magnetization for a 10 mT out-of-plane field.

photoelectron kinetic energy E_{kin} , the perpendicular momentum is given by:

$$\mathbf{k}_z = \sqrt{\frac{2m_e (E_{\text{kin}} - V_{000})}{\hbar^2}} - \mathbf{k}_{\parallel} + \mathbf{p}_{\gamma,z}, \quad (\text{S1})$$

where m_e is the electron mass, \mathbf{k}_{\parallel} the in-plane momentum, V_{000} the inner potential and $\mathbf{p}_{\gamma,z}$ the component of the photon momentum ($\hbar\nu/c$) perpendicular to the sample surface [?]. The inner potential is a material and energy dependent parameter. We have estimated it by comparing the measured band structure with the expected periodicity of the Brillouin zone (cf. Fig. 1(f) in the main paper). We used a value of $V_{000} \approx 10$ eV, which gives a fair agreement between theory and experiment, but slightly differs from the previously used $V_{000} = 16(1)$ eV [S3].

Static charging

Because $2H$ -MoTe $_2$ is a semiconductor, it tends to statically charge upon x-ray irradiation at low temperature. This is shown in Fig. S3, which displays the binding energy of several features in the band structure as a function of photon flux. The binding energies were calibrated by measuring the Fermi level of Au. For some measurements the

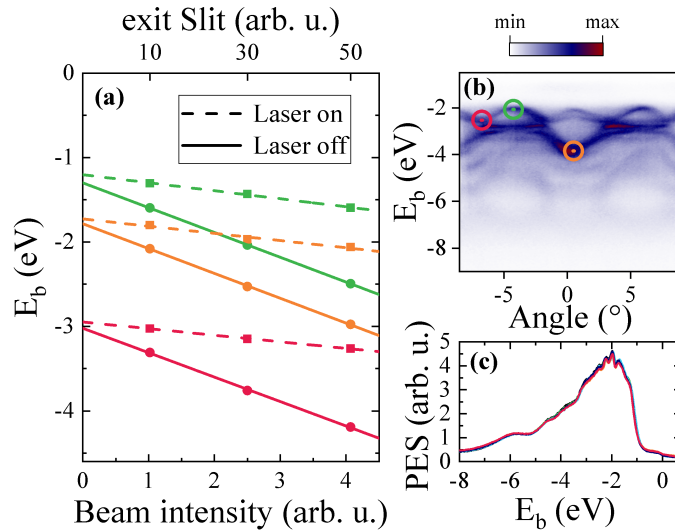


FIG. S3: (a) Binding energy of several features indicated in (b) as a function of x-ray flux. (c) Angle integrated spectra corresponding to (a), after rigidly aligning the valence band maximum.

sample was additionally irradiated with a near UV laser. This excites some charge carriers and helps to significantly reduce the charging (Fig S3(a)). In both cases, the charging can be assumed to be a rigid shift of the spectrum. This is evident from the linear dependence on the flux in Fig S3(a) and from the collapse of angle integrated spectra after alignment of the valence band maximum in Fig S3(c). Therefore, in the main paper we only show the binding energy with respect to the valence band maximum.

n-type samples

All measurements shown in the main text were performed on samples that were freshly cleaved in-situ at ~ 12 K directly before the measurement. However, after a couple of hours of ARPES measurements the $2H$ -MoTe₂ samples usually degrade and the material becomes slightly *n*-type. This is exemplified by the spectra in Fig. S4, where a small spectral weight above the valence band was observed. These measurements clearly confirm that the band gap

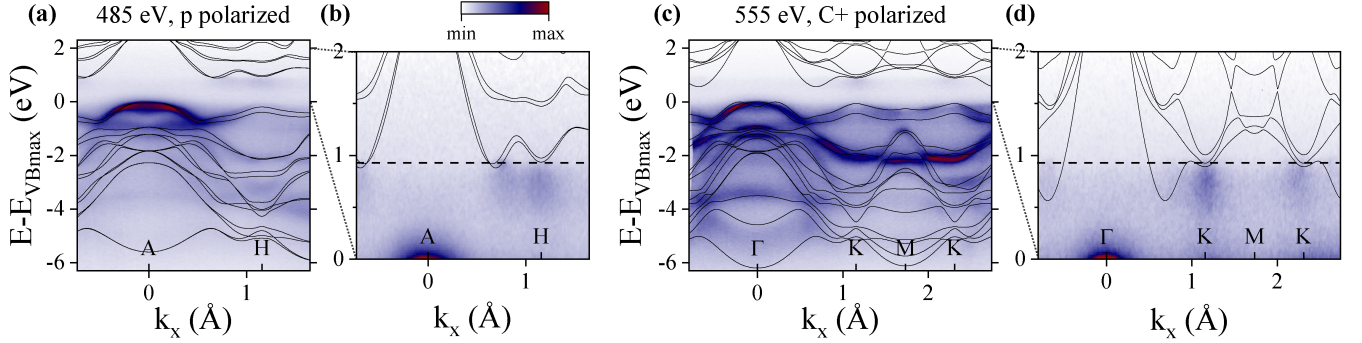


FIG. S4: (a,c) Spectra measured on a sample that became *n*-type over time. (b,d) Zooms into the region above the valence band maximum. The dashed line indicates the estimated, effective position of the Fermi level.

in $2H$ -MoTe₂ is indirect.

Density-functional theory calculations

Details of the calculated stable muon positions are listed in Tab. II. We further show the local spin density of states

Species	Wyckoff position	frac.	coordinates	ΔE (eV)	ZPE (eV)
μ^+	2b	0	0 0.25	0	0.57
μ^+	6g	0.5	0 0.5	1.5	0.22
Mu	2b	0	0 0.25	0	0.54
Mu	2a	0	0 0.5	1.24	0.26

TABLE II: Details of the identified stable and meta-stable site for several implanted probe species. ΔE denotes the difference in the total energy of the relaxed supercell compared to the most stable site and ZPE is the approximate ground state energy of the muon.

at the different stopping sites in Fig. S5. It is evident from this figure, that there is no induced magnetism at the stable muon stopping site **b** and **g**, see Fig. S5(b,f). For site **b**, the absence of an induced spin polarization can be understood because of the strong pairwise interaction of the muon with the neighboring Mo atoms. However, in the case of a muonium (and also a muon) sitting at the hexagonal site inside the vdW gap (site **a**) and when employing a finite Hubbard term U , a significant spin density is induced, see Fig. S5(c,d). This is very similar to what was found for hydrogen adsorbed on a monolayer $2H$ -MoTe₂ or on graphene [S4, S5]. Note that site **a** is only a stable stopping site of muonium but not of a muon. As argued in more detail in the main text, such a muonium induced magnetic state can explain the observed coherent muon spin precession, while being consistent with the absence of a magnetic signal in magnetization and ^{125}Te -NMR.

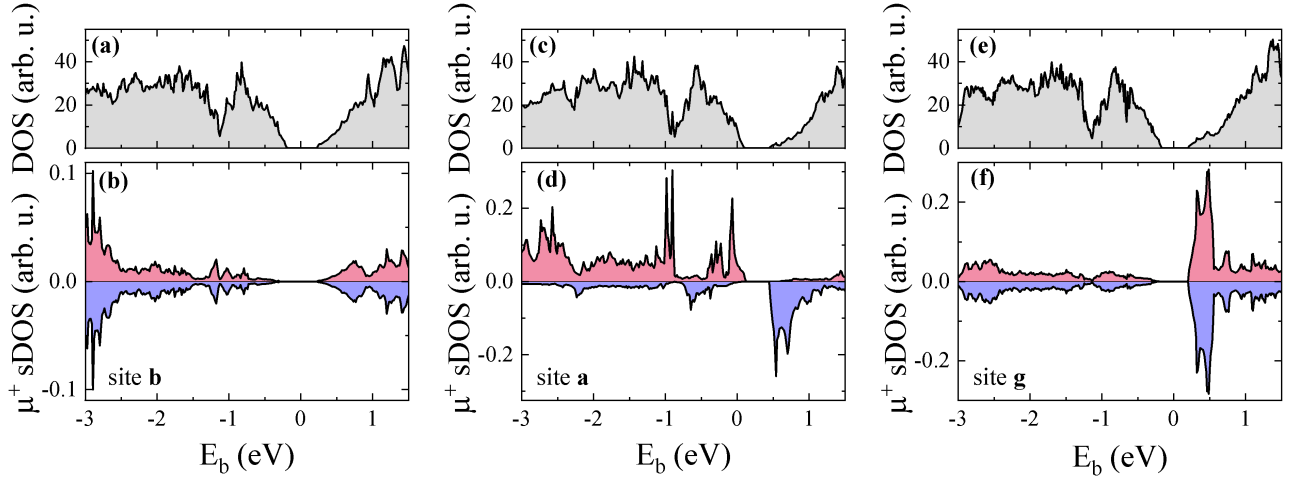


FIG. S5: Total density of states and local spin density of states calculated for a muon (i.e. a hydrogen potential in a charged supercell) at site **b** (a,b), site **a** (c,d), and site **g** (e,f), respectively. Note that site **a** is not a stable stopping site for a diamagnetic muon.

Muon spin spectroscopy

Zero field angle dependence

In order to determine the variation in the zero field (ZF) μ SR spectra as a function of sample orientation, the asymmetry spectra (such as the ones shown in Fig. 1(b,c) of the main paper) were fitted to a sum of a Gaussian damped oscillating part and two exponentially damped components:

$$A(t) = A_1 e^{-\frac{1}{2}(\sigma t)^2} \cos(\gamma_\mu B t + \varphi) + A_2 e^{-\lambda_{\text{slow}} t} + A_3 e^{-\lambda_{\text{fast}} t}. \quad (\text{S2})$$

We further assumed that the internal field B and the depolarization rate σ of the oscillating part to be independent of the measured projection of the polarization. Figure S6 shows the resulting oscillating ZF asymmetry A_1 in different sets of detectors (corresponding to different projections of the muon spin polarization) as a function of the sample orientation. In order to understand this rotation dependence, one has to consider the Larmor precession of the muon

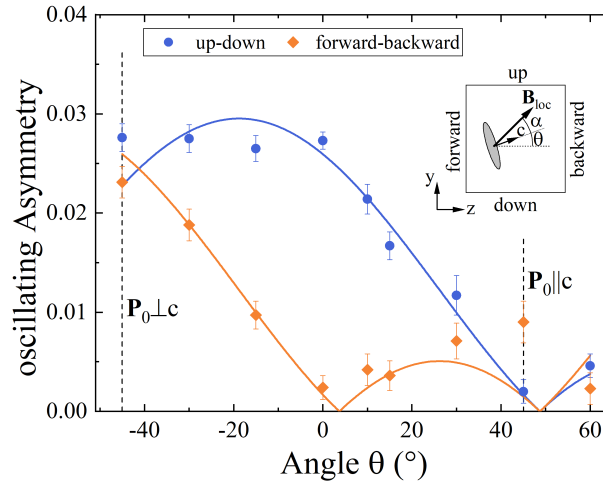


FIG. S6: Oscillating asymmetry in different sets of detectors, measured for different orientations of the sample. The inset depicts the measurement geometry.

polarization $\mathbf{P}(t)$, defined as

$$\frac{d\mathbf{P}(t)}{dt} = \gamma_\mu \mathbf{P}(t) \wedge \mathbf{B}. \quad (\text{S3})$$

Here, \mathbf{B} denotes the local magnetic field vector and $\gamma_\mu = 2\pi \times 135.5 \text{ MHz/T}$ is the gyromagnetic ratio of the muon. The resulting precession can be written as [S6, S7]:

$$\mathbf{P}(t) = \mathbf{p}^\parallel + \mathbf{p}_1^\perp \cos(\gamma_\mu B t) + \mathbf{p}_2^\perp \sin(\gamma_\mu B t), \quad (\text{S4})$$

$$\mathbf{p}^\parallel = \frac{(\mathbf{P}_0 \cdot \mathbf{B})\mathbf{B}}{B^2}, \quad \mathbf{p}_1^\perp = \mathbf{P}_0 - \mathbf{p}^\parallel, \quad \mathbf{p}_2^\perp = \mathbf{p}_1^\perp \wedge \frac{\mathbf{B}}{B}, \quad (\text{S5})$$

where \mathbf{P}_0 is initial polarization vector and $B = \|\mathbf{B}\|$ denotes the magnitude of the field.

We choose the coordinate system (x, y, z) depicted in the inset of Fig. S6, with $\mathbf{P}_0 \propto (0, 1, 1)$, and the local field $\mathbf{B} = B(0, \sin(\theta + \alpha), \cos(\theta + \alpha))$. The angle θ denotes the rotation of the sample's c -axis with respect to the detectors and α is a hypothetical offset between the local magnetic field seen by the muon and the c -axis of the crystal.

The asymmetry probed by a set of opposite detectors is proportional to the projection of the polarization along that direction. Therefore, in the inset of Fig. S6 the asymmetry in the up-down detectors is $A_{\text{up-do}} \propto \mathbf{P}(t) \cdot \hat{\mathbf{e}}_y$, and the one in the forward backward detectors $A_{\text{fw-ba}} \propto \mathbf{P}(t) \cdot \hat{\mathbf{e}}_z$, where $\hat{\mathbf{e}}_y$ and $\hat{\mathbf{e}}_z$ are the unit vectors in the y and z directions.

Inserting these conventions into Eq. S4, we find that the oscillating part of the asymmetry is given by \mathbf{p}_1^\perp and that accordingly

$$A_{\text{up-do}} \propto 1 - \sqrt{2} \sin(\alpha + \theta + \pi/4) \sin(\theta + \alpha), \quad (\text{S6})$$

$$A_{\text{fw-ba}} \propto 1 - \sqrt{2} \sin(\alpha + \theta + \pi/4) \cos(\theta + \alpha). \quad (\text{S7})$$

These curves are depicted as solid lines in Fig. S6, where $\alpha = -4(1)^\circ$ was determined using nonlinear least-squares optimization. As the sample was aligned with respect to the detector frame by hand, this small value of α could easily correspond to a small misalignment of the sample. Therefore, we conclude that within our measurement precision, the local field points along the c -axis of the crystal.

Low energy μSR

We also investigate the evolution of the observed magnetism within $\sim 100 \text{ nm}$ from the surface using low energy μSR . In particular, we tune the implantation depth of the muons by varying their implantation energy, E (Fig. S7(b)). At

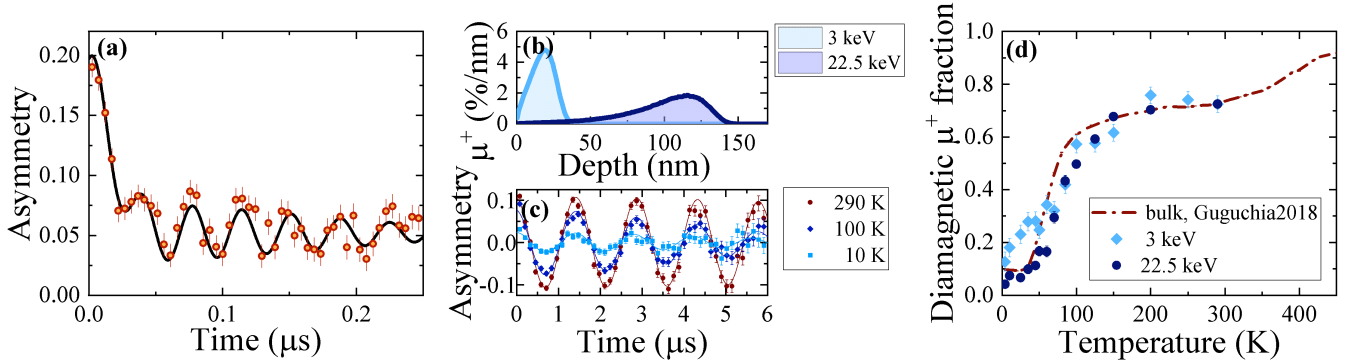


FIG. S7: (a) μSR time spectrum measured in zero field at 10 K with an implantation energy of 22.5 keV. (b) Simulated implantation profiles for different implantation energies. The average stopping depths beneath the surface for 3 keV or 22.5 keV are 18 nm and 99 nm, respectively. (c) Representative weak transverse field asymmetry spectra at 22.5 keV corresponding to (d). (d) Fraction of diamagnetic muons as a function of temperature, normalized at RT. The dashed line shows the bulk data from Ref. [S1]. The solid lines in (a,c) show fits to the data.

10 K and $E = 22.5 \text{ keV}$ (corresponding to an average implantation depth of 99 nm), the muon spins exhibit a coherent precession in zero field (ZF) similar to what we observed in the bulk, see Fig. S7(a). This spectrum was fitted to the following function:

$$A(t) = A_1 e^{-\frac{1}{2}(\sigma_{\text{osc}} t)^2} \cos(\gamma_\mu B_{\text{int}} t) + A_2 e^{-\lambda_{\text{slow}} t} + A_3 e^{-\frac{1}{2}(\sigma_{\text{fast}} t)^2}. \quad (\text{S8})$$

The first term describes the muons that oscillate in a local magnetic field B_{int} . The second term represents the slowly depolarized (nonmagnetic) signal and the third accounts for the strongly damped part due to background contribution from muons stopping in the Ni coated sample plate. This analysis is similar to that used in Ref. [S1], except for the background contribution. We find that the oscillation frequency in Fig. S7(a) corresponds to an internal static field $B_{\text{int}} = 200(2)$ mT. Within the statistical error of the measurement, this is consistent with what is found in the bulk [S1].

We then use a small magnetic field (5 mT, transverse to the initial muon spin) to identify the fraction of diamagnetic muons, which is proportional to the non-magnetic fraction of the sample [Fig. S7(c,d)]. These spectra were fitted with a single, Gaussian damped oscillating polarization.

$$A(t) = A_0 e^{-\frac{1}{2}(\sigma t)^2} \cos(\gamma_\mu B t). \quad (\text{S9})$$

This function only describes the muons in a nonmagnetic environment oscillating at a frequency close to the Larmor frequency in the applied field. Any magnetic or strongly damped signal (cf. Eq. S8) leads to an effective loss of A_0 . The background contribution to A_0 was determined by measuring an empty Ni plate with the same beamline settings. This temperature independent value was subtracted from the measured A_0 and the resulting curve is shown in Fig. S7(d). Independent of depth and within the experimental uncertainties, all points in Fig. S7(d) closely follow the bulk behavior reported in Ref. [S1]. Therefore, we conclude that the bulk magnetic properties observed with μSR in $2H\text{-MoTe}_2$ do not change in the near surface region of the crystals.

¹²⁵Te-NMR

Powder line shapes

Figure S8 shows the detailed temperature dependence of the powder line shape of $2H\text{-MoTe}_2$ in 7.067 T. Similar to the spectra of the single crystal measurements shown in the main part of the paper, here, too, we observe no significant peak-shift or broadening, that would be the two common fingerprints of a magnetic transition. We note that there are some small changes in the line shape as a function of temperature. However, these are most likely due to a change in spectral weight between different portions of the resonance line, owing to a difference in their spin-lattice relaxation (SLR) temperature dependence. Note that a similar SLR variation along different crystallographic directions has been observed in ¹²⁵TeNMR in $1T\text{-ZrTe}_2$ [S8].

Spin-lattice relaxation

The spin-lattice relaxation rate T_1^{-1} of the ¹²⁵Te moments measured on the oriented single crystals is shown in Fig. S9. At high temperature, the SLR shows an exponential dependence on temperature ($1/T_1 \propto e^{\Delta/T}$). This is a typical behavior observed in semiconductors. However, we find that here the gap $\Delta = 27.7(3)$ meV is much smaller than the spectroscopic band gap, which is on the order of ~ 1 eV, cf. Fig. S4. This difference is likely due to, e.g., the presence of a small amount of impurity-induced in-gap states, which have too little spectral weight to be detected with ARPES, but still can depolarize the ¹²⁵Te nuclear spins. At present, we are unable to determine the mechanism for the increase in relaxation rate at low temperatures in $2H\text{-MoTe}_2$. However, we note that a similar increase in relaxation was observed in the analogue compounds ZrTe_2 and ZrSiTe [S8, S9]. In both cases, the increase in relaxation rate is suggested to arise from a contribution from Dirac electrons. However, $2H\text{-MoTe}_2$ is not a Dirac system, so the fact that there is a similar increase in relaxation rate suggests that the true origin of this effect might be due to some new mechanism, yet to be understood.

Time scales probed by μSR and ¹²⁵Te-NMR

The muon with a lifetime of $\sim 2.2 \mu\text{s}$ probes the system on a MHz (and faster) time scale. On the other hand, ¹²⁵Te-NMR is predominantly sensitive to fluctuations at the ¹²⁵Te-Larmor frequency, which in an applied field of 7 T is ~ 95 MHz. Therefore, if the system were magnetically ordered, both techniques should be able to detect this equally. NMR is also sensitive to much longer relaxation times. The slow SLR of $1/T_1 < 1 \text{ ms}^{-1}$ observed at low temperatures is far outside the μSR time window. But we note that the SLR in Fig. S9 has a minimum around 40 K, i.e., the onset temperature of the magnetic oscillations observed by μSR . However, the temperature dependence of the previously reported μSR data (Fig. 1(c) of Ref. [S1]) suggests a second order magnetic transition. Therefore, in the presence of

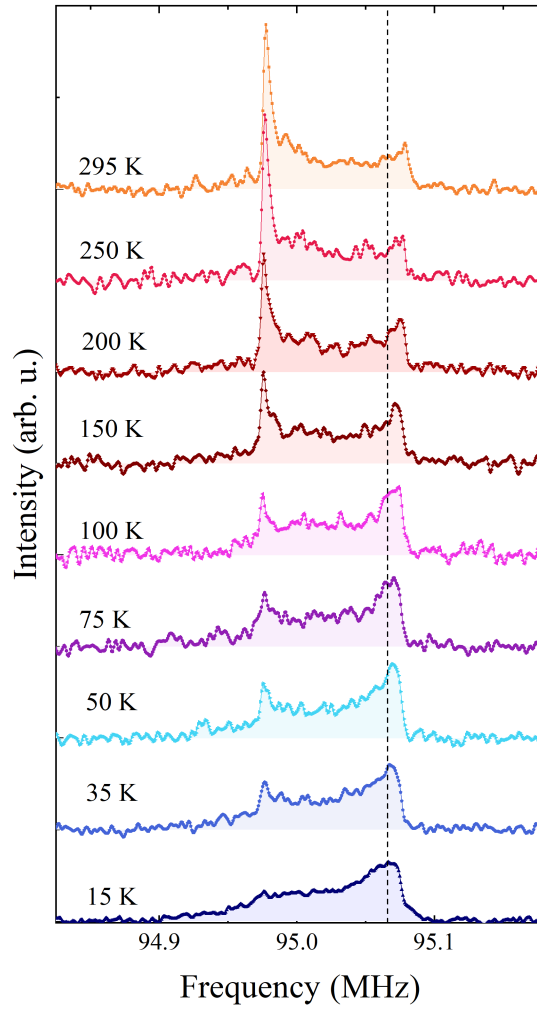


FIG. S8: ^{125}Te -NMR powder line shapes of $2H\text{-MoTe}_2$ in a field of 7.067 T at different temperatures. The spectra have been offset for clarity. The black dashed line indicates the expected position of the reference line.

such a transition, the SLR should instead show a peak at this temperature due to critical magnetic fluctuations. This finding confirms once more that the observed local magnetic field in μSR is not intrinsic to $2H\text{-MoTe}_2$.

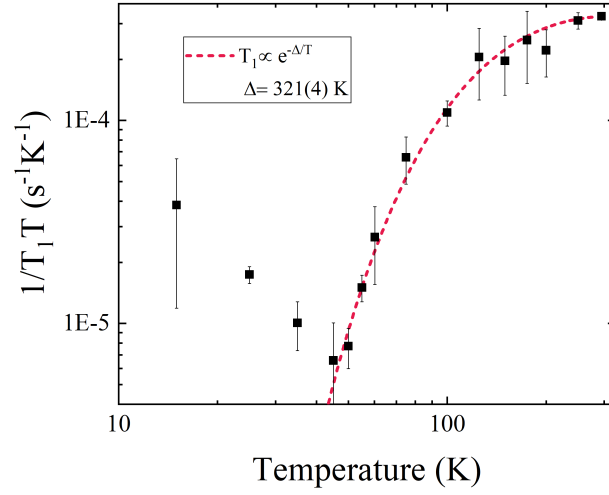


FIG. S9: ^{125}Te -NMR spin lattice relaxation rate in $2H\text{-MoTe}_2$ in a field of 7.067 T as a function of temperature. The dashed line indicates the activated Arrhenius-like behavior at high temperature.

-
- [S1] Z. Guguchia, A. Kerelsky, D. Edelberg, S. Banerjee, F. v. Rohr, D. Scullion, M. Augustin, M. Scully, D. A. Rhodes, Z. Shermadini, et al., *Science Advances* **4**, eaat3672 (2018).
- [S2] S. Tongay, S. S. Varnoosfaderani, B. R. Appleton, J. Wu, and A. F. Hebard, *Applied Physics Letters* **101**, 123105 (2012).
- [S3] T. Böker, R. Severin, A. Müller, C. Janowitz, R. Manzke, D. Voß, P. Krüger, A. Mazur, and J. Pollmann, *Physical Review B* **64**, 235305 (2001).
- [S4] Y. Ma, Y. Dai, M. Guo, C. Niu, J. Lu, and B. Huang, *Physical Chemistry Chemical Physics* **13**, 15546 (2011).
- [S5] H. González-Herrero, J. M. Gómez-Rodríguez, P. Mallet, M. Moaied, J. J. Palacios, C. Salgado, M. M. Ugeda, J.-Y. Veuillen, F. Yndurain, and I. Brihuega, *Science* **352**, 437 (2016).
- [S6] M. Herak, A. Zorko, M. Pregelj, O. Zaharko, G. Posnjak, Z. Jagličić, A. Potočnik, H. Luetkens, J. van Tol, A. Ozarowski, et al., *Physical Review B* **87**, 104413 (2013).
- [S7] A. Yaouanc and P. de Réotier, *Muon Spin Rotation, Relaxation, and Resonance: Applications to Condensed Matter*, International Series of Monographs on Physics (OUP Oxford, 2011), ISBN 978-0-19-959647-8.
- [S8] Y. Tian, N. Ghassemi, and J. H. Ross, *Physical Review B* **102**, 165149 (2020).
- [S9] Y. Tian, Y. Zhu, R. Li, Z. Mao, and J. H. Ross, *Physical Review B* **104**, L041105 (2021).
- [S10] V. N. Strocov, X. Wang, M. Shi, M. Kobayashi, J. Krempasky, C. Hess, T. Schmitt, and L. Patthey, *Journal of Synchrotron Radiation* **21**, 32 (2014).
- [S11] The formulas for the specific measurement geometry can be found in Ref. [S10]